Functional Dynamics of the Hydrophobic Cleft in the N-Domain of Calmodulin

Dominico Vigil,* Stephen C. Gallagher,[†] Jill Trewhella,[†] and Angel E. García*

*Theoretical Biology and Biophysics Group, T10 MS K710, and [†]Biosciences Division, Los Alamos National Laboratory, Los Alamos, New Mexico 87545 USA

ABSTRACT   Molecular dynamics studies of the N-domain (amino acids 1–77; CaM_{1-77}) of Ca^{2+}-loaded calmodulin (CaM) show that a solvent exposed hydrophobic cleft in the crystal structure of CaM exhibits transitions from an exposed (open) to a buried (closed) state over a time scale of nanoseconds. As a consequence of burying the hydrophobic cleft, the R_g of the protein is reduced by 1.5 Å. Based on this prediction, x-ray scattering experiments were conducted on this domain over a range of concentrations. Models built from the scattering data show that the R_g and general shape is consistent with the simulation studies of CaM_{1-77}. Based on these observations we postulate a model in which the conformation of CaM fluctuates between two different states that expose and bury this hydrophobic cleft. In aqueous solution the closed state dominates the population, while in the presence of peptides, the open state dominates. This inherent flexibility of CaM may be the key to its versatility in recognizing structurally distinct peptide sequences. This model conflicts with the currently accepted hypothesis based on observations in the crystal structure, where upon Ca^{2+} binding the hydrophobic cleft is exposed to solvent. We postulate that crystal packing forces stabilize the protein conformation toward the open configuration.

INTRODUCTION

The EF-hand family of proteins contains more than 200 calcium-binding proteins that act as Ca^{2+} sensors and regulators in the cell. The EF-hand motif consists of a helix-loop-helix structure that binds Ca^{2+} in the loop region. It has long been held that members of the Ca^{2+}-sensor subset of this family translate a transient increase in cellular Ca^{2+} levels into a mechanical or metabolic response by exhibiting a conformational change in response to Ca^{2+} binding, which in turn facilitates regulation of target proteins (Kawasaki et al., 1998). The EF-hand proteins are involved in a large number of cellular activities, including cell cycle control, neurotransmitter release, and muscle contraction, and are implicated in diseases such as cancer and Alzheimer's disease (Vito et al., 1996; Hait and Lazo, 1986).

Calmodulin (CaM) is a highly conserved, 148-residue, EF-hand protein that regulates many cellular targets including a number of kinases, cyclases, calcineurin, nitrous oxide synthase, and phosphodiesterase (Crivici and Ikura, 1995). CaM binds four Ca^{2+}, which results in a modulation of its interactions with target proteins to effect activation or inactivation of numerous biochemical pathways (James et al., 1995). The crystal structure of Ca^{2+}-bound CaM has been solved and shows an unusual dumbbell-shaped molecule with two globular lobes, called the N- and C-domains, separated by a single seven-turn, solvent-exposed α-helix. The two domains are in a *trans* orientation with the central helix fully extended. Each domain contains two EF-hand

motifs that serve to bind Ca^{2+}. Each of these paired EF-hand structures form a cup-shaped structure, with two Ca^{2+}-binding loops at the base and four helices at the sides. The inner surface of each cup shaped domain forms a cleft that is lined with hydrophobic residues that are exposed to the solvent in the crystal structure (Babu et al., 1985, 1988; Chattopadhyaya et al., 1992). Small-angle x-ray scattering and NMR relaxation data on CaM in solution have shown that, on average, the N- and C-domains are closer together than in the crystal structure and that the central helix linker is flexible (Heidorn and Trewhella, 1988; Barbato et al., 1992). Scattering experiments of CaM complexed with the CaM-binding sequence from skeletal muscle myosin light chain kinase (MLCK) revealed a highly compacted shape compared to free CaM (Heidorn et al., 1989). Crystal structure and NMR results of CaM complexed with peptide sequences corresponding the CaM-binding domains in smooth and skeletal muscle MLCKs, respectively, show the compacted structure has the N- and C- domains in a *cis* conformation (Meador et al., 1992; Ikura et al., 1992), with the hydrophobic clefts on each domain holding the peptide. The peptides form an amphipathic helix in the complex. NMR structures of apo CaM show that each of the individual domains is more compact than in the Ca^{2+}-bound form, with the four helices wrapped around each other more tightly. In this configuration, there is no exposure of hydrophobic residues to solvent (Kuboniwa et al., 1995; Zhang et al., 1995; Finn et al., 1995). This observation supported the earlier interpretations of the crystal structure of the evolutionarily related skeletal muscle troponin C which had only one of its two domains loaded with Ca^{2+} (Herzberg et al., 1986).

Therefore, it is widely believed that Ca^{2+} binding to CaM causes an opening of the hydrophobic cleft via a rearrangement of helices within each domain such that hydrophobic

residues key to target protein binding are exposed (Zhang and Yuan, 1998). The central helix is then believed to flex so that the N- and C-domains can engulf a target binding sequence, forming hydrophobic and electrostatic interactions that contribute to the high binding affinity (in nM) (Crivici and Ikura, 1995). In particular, methionine and phenylalanine residues in the hydrophobic clefts have been implicated as important for interactions with target binding sequences (Gellman, 1991; O'Neil and Degrado, 1990). This mode of binding involving residues within the hydrophobic cleft of Ca^{2+}-bound CaM interacting with an amphipathic helical target sequence is characteristic of a large number of CaM-target protein interactions (O'Neil and Degrado, 1990).

Much of the previous computational work on CaM was done to address issues concerning the relative positions of the N- and C-domains and the nature of the central helix. Molecular dynamics simulations of CaM in solution supported the ideas that the central helix is flexible and that there is a large amount of conformational space available to Ca^{2+}-bound CaM, ranging from the extended crystal structure to the more compact structure suggested by scattering studies to the highly compacted structures observed in the complexes with peptides (Mehler et al., 1991; Weinstein and Mehler, 1994). A more recent 3-ns molecular dynamics simulation of Ca^{2+}-bound CaM has been performed (Wriggers et al., 1998). This simulation began with the crystal structure; halfway through the simulation, the central helix unwound and bent at residue 74. The two domains then adopted a *cis* conformation in preparation for target binding, as suggested by scattering measurements and the crystal structures.

There remain many unresolved issues concerning the structure-function relationship of CaM. The full breadth of target binding sequences and their structural motifs is not known, nor is there full understanding of the basis for this highly conserved and relatively small protein's ability to bind with high affinity and specificity to such a diverse array of targets in the cell. Analysis of the conformational disorder in a 1 Å resolution Ca^{2+}-bound CaM structure, Wilson and Brunger (2000) found that 16 amino acids in the hydrophobic cleft region sample alternative conformations. This plasticity of the hydrophobic cleft has been associated with the binding of target peptides to CaM. Wilson and Brunger (2000) have also suggested that a moderate degree of overall packing in the hydrophobic clefts observed in this high-resolution structure may be evolutionarily optimized to achieve a large number of conformational substates.

To investigate in detail the nature of the dynamics within an individual domain of CaM and its possible relationship to target binding, we performed molecular dynamics simulations of apo N-domain of CaM (nCaM), Ca^{2+}-bound nCaM, and Ca^{2+}-CaM. We compared the dynamics of the apo nCaM with Ca^{2+}-bound nCaM to evaluate the possible functional relevance of the protein dynamics. We first performed simulations with nCaM instead of the whole protein. This simplification is justified, as it has been shown that the two domains of CaM are independent in the absence of bound target peptides on the nanosecond time scale of the simulations (Barbato et al., 1992). We were mostly interested in the details of the hydrophobic cleft conformation of Ca^{2+}-bound nCaM and whether it persists in solution. In a 3-ns simulation, the nCaM domain quickly closes its hydrophobic cleft, which remains closed for the rest of the simulation. In another 1-ns simulation, the cleft quickly closes and opens up again. Small-angle x-ray scattering experiments are performed on apo-nCaM and Ca^{2+}-bound nCaM in order to investigate its average solution configuration. These data clearly distinguish the open and closed conformations, and support the prediction of the simulations. Importantly, it appears that in solution apo nCaM *and* Ca^{2+}-bound nCaM are, on average, in a closed conformation, suggesting that the residues in the hydrophobic cleft are, on average, protected from solvent. The effect of Ca^{2+} binding appears to be to decrease mobility in the Ca^{2+} loop regions of the structure while increasing the large amplitude motions of the helices with respect to each other, providing transient, open configurations that would favor target binding. It appears that the open configuration observed in the crystal structure for the N-domain of Ca^{2+}-bound CaM may be stabilized by crystal packing forces.

METHODS

Description of the system and simulations

Four molecular dynamics simulations are performed: two of the Ca^{2+}-loaded nCaM, one of the entire Ca^{2+}-loaded CaM, and one of the apo nCaM. We assume that the two lobes of CaM act independently on the nanosecond time scale, so the N-domain alone acts as it would in the whole CaM. AMBER 4.1 energy minimization and molecular dynamics software are used (Pearlman et al., 1995). The all-atom force field (Cornell et al., 1995) and PME (particle mesh Ewald) algorithm implemented in AMBER 4.1 is used to model electrostatic interactions (Darden et al., 1993). All the simulations are carried out at constant N, T, and P, with $P = 1$ atm and $T = 300$ K.

The two separate simulations of Ca^{2+}-loaded nCaM (residues 1–77) are started from the crystal structure of human CaM (Chattopadhyaya et al., 1992). Residues 1–3, missing from the crystal structure, are modeled to be in favorable steric positions, and residues 78–147 are deleted from the simulation. The nCaM in vacuum is subjected to 500 cycles of steepest descent energy minimization. Counterions are then placed in random positions around the protein, at least 5 Å away from protein atoms or other ions to balance the $-6e$ charge of the protein and to approach physiological salt concentrations. The system is then solvated to fill a cubic box of 56.4 Å on each side. Five hundred cycles of steepest descent energy minimization are performed, followed by two simulations, one lasting 3.040 ns and the other 1.150 ns. These two simulations start from the same minimized configuration and are identical in all ways except for starting velocities. The resulting system has a total of 15471 atoms, including 1173 protein atoms, two Ca^{2+}, 20 K^+ and 14 Cl^- ions, and 4754 TIP3P water molecules. The concentrations for the counterions are $[K^+] = 0.18$ M and $[Cl^-] = 0.13$ M. The real part of the Ewald electrostatic potential is cut off at 9 Å. The reciprocal space part of the Ewald potential is calculated on a

cubic grid of 48 points on the side and interpolated over all space with a cubic spline.

For the whole Ca^{2+}-bound CaM (residues 1–147) simulation, the same crystal structure is used as in the initial configuration (Chattopadhyaya et al., 1992). Again the first three residues are modeled, and residue 148, missing in the crystal structure, is excluded. Counterions are added to neutralize the $-25e$ charge on the protein. This system is then solvated to fill a box with dimensions $82 \times 65 \times 49$ Å. Five hundred steps of steepest descent energy minimization are performed, followed by 2.035 ns of molecular dynamics. The system has a total of 26115 atoms, including 2240 protein atoms, 7934 TIP3P water molecules, 4 Ca^{2+}, 43 K^+ and 26 Cl^- ions. The concentrations for the counterions are $[K^+] = 0.27$ M and $[Cl^+] = 0.16$ M. The real part of the Ewald electrostatic potential is cut off at 9 Å. The reciprocal space part of the Ewald potential is calculated on a grid of $81 \times 64 \times 48$ points and interpolated over all space with a cubic spline.

A simulation of apo (Ca^{2+}-free) nCaM is also performed. The simulation starts from the reported NMR structure closest, in *rmsd*, to the average NMR structure of CaM (31). Again only residues 1–77 are used for the simulation. The total charge on the protein is $-10e$, so we add 20 K^+ and 10 Cl^- ions. This system is then solvated in a box with dimensions $54 \times 46 \times 50$ Å. A total of 500 cycles of steepest descent energy minimization are performed, followed by 2.51 ns of molecular dynamics, of which the last 2.2 ns are used for analysis. The resulting system has a total of 12033 atoms, including 1204 protein atoms, 3600 TIP3P water molecules, 20 K^+ ions, and 10 Cl^- ions. The concentrations of the K^+ and Cl^- ions are 0.27 M and 0.135 M, respectively. The real part of the Ewald electrostatic potential is cut off at 9 Å. The reciprocal space part of the Ewald potential is calculated on a cubic grid of 56 points on the side and interpolated over all space with a cubic spline.

Principal component analysis

To study the large-amplitude motions of the protein from the simulations, we find a set of directions for each atom that represents the best fit to the locations of an atom from different configurations along the simulation trajectories. These directions are chosen such that the mean square distance from the different configurations of an atom to the principal component coordinates is minimized. One can then follow the principal component coordinates, and even next few components, to gain information about the important large-scale motions of the protein. Analysis of these principal component coordinates allows a dissection of the vast trajectories into the major global conformational changes during a simulation. The details of construction of principal component coordinates have been previously described (García, 1992; García et al., 1997). A total of 598 non-hydrogen protein atoms are included in this analysis.

Radial distribution functions

To calculate water and counterion coordination to various groups in the protein, radial distribution functions (rdf) were used. We calculate the proximity rdf (Mehrotra and Beveridge, 1980) by generating histograms of the number of water molecules or ions that are closest and within spheres of increasing radii to the reference atom. These distributions are then normalized by the number of waters uniformly distributed within the spherical shells around a reference point. The proximity coordination of water molecules or ions around a specific protein atom is obtained by integrating the radial distribution function within a sphere that encompasses the first hydration or ion coordination shell. The sum of the proximity water coordination number over all protein atoms gives the total number of waters coordinated to the protein.

Small-angle x-ray scattering

Small-angle x-ray scattering measurements

Samples of nCaM are purified as described previously (Finn et al., 1995). The protein is dialyzed twice against 1000 volumes of 25 mM MOPS buffer, pH 7.5 containing 100 mM KCl and a fivefold molar excess of $CaCl_2$. X-ray scattering data are collected using the small-angle x-ray instrument described previously (Heidorn and Trewhella, 1988). Samples are maintained at 16°C during data acquisition. The scattering from protein molecules is calculated by subtracting data from a buffer blank from that for the protein in buffer, each recorded under identical conditions in the same sample cell and normalized to constant beam monitor counts.

Data analysis

Data are summed from detector channels at scattering angles of equal magnitude on opposite sides of the direct beam for analysis described previously (Heidorn and Trewhella, 1988). Parameters used for analysis of scattering data include R_g, maximum linear dimension of the particle (d_{max}), and molecular volume (V). For a dilute solution of monodispersed, identical particles, the scattering intensity, $I(Q)$, and $P(r)$, the probable frequency of vector lengths connecting small-volume elements within the scattering particle, are related by a Fourier transformation:

$$P(r) = \frac{r^2}{2\pi^2} \int I(Q) Q^2 \frac{\sin(Qr)}{Qr} \, dQ \qquad (1)$$

where $Q = (4\pi sin\theta)/\lambda$ is the amplitude of the scattering vector, θ is half the scattering angle, and λ is the wavelength of the scattering radiation, 1.54 Å. $P(r)$ is calculated from the experimental scattering profile using the indirect Fourier transform method (Moore, 1980). $P(r)$ goes to zero at the d_{max} of the particle (Heidorn and Trewhella, 1988). R_g is calculated as the second moment of $P(r)$.

X-ray scattering model calculations

The atomic mass distribution in nCaM in the apo and the Ca^{2+}-bound states are modeled using Monte Carlo methods previously published (Zhao et al., 1998). The data were modeled using the program SASMODEL with an initial starting model configuration that allows rapid generation and testing of arbitrary shapes with very few constraints. In summary, the program SASMODEL generates a chain of ellipsoids whose total volume is constrained to be approximately that of the protein being modeled. The semi-axes of each ellipsoid are chosen randomly within a defined set of ranges. For these calculations 30 ellipsoids are used, 15 with semi-axis dimensions ranging from 3 to 7 Å and 15 with semi-axis dimensions 0 to 15 Å (seven of these more asymmetric ellipsoids are placed at the start of the chain and 8 at the end). The conformation of the chain is randomly selected by rotating each ellipsoid about its origin, defined as the tip of the previous ellipsoid. The rotation applies the first two of three possible Euler rotations, using random angles chosen uniformly over the available range. Eliminating the last Euler rotation guarantees that at least one semi-axis of each ellipsoid is within the *x-y* plane of the model and aids in generating relatively compact mass distributions. The model is thus constrained to be contiguous, but flexible enough to be able to generate many random shapes. Model I(Q) profiles are calculated by filling the model shapes with a uniform distribution of randomly placed points. Points are saved in Brookhaven PDB format for export to standard visualization programs. The vector length distribution $P(r)$ is directly calculated from the points, assuming identical scatterers (this calculation is the rate-limiting step), and $P(r)$ is transformed in accordance with scattering theory to yield $I(Q)$. The

model is evaluated against experimental data using a reduced χ^2 value,

$$\chi^2 = \frac{1}{N} \sum_N \frac{(I_{obs} - I_{calc})^2}{\sigma^2}, \qquad (2)$$

where N is the number of data points in the scattering profile, I_{obs} and I_{calc} are the observed and calculated scattering intensities, and σ is the error in I_{obs}. The model with the lowest χ^2 value is saved. A best-fit model with a χ^2 of 1.0 is considered a perfect fit within the errors of the data.

We have used these Monte Carlo-based modeling methods extensively with single-ellipsoid or two-ellipsoid model approximations (Zhao et al., 1998; Krueger et al., 1997; Zhi et al., 1998; Gallagher et al., 1999; Wall et al., 2000). This approach is one of a number available for modeling scattering data (see, for example, Chacon et al., 2000; Svergun, 1999). Each approach performs with similar success, generally predicting R_g values and protein shapes in solution with high precision and reliability. The arbitrary shape procedure used here has been developed in an independent program written for simplification and ease of distribution (ELLMODEL, available upon request from M. E. Wall, mewall@lanl. gov). The modeling for nCaM data presented here used scattering data in the Q-range of 0.006 to 0.2 Å^{-1}.

RESULTS

Simulations on the Ca^{2+}-saturated CaM

The principal component analysis is performed for configurations collected over the last 3.0 ns of Ca^{2+}-loaded nCaM simulation. Fig. 1 *A* shows the displacement of the optimal mode of the MD trajectory. In this analysis, for reasons discussed below, only the principal mode is described. One can see that during the first 0.5 ns there is a quick displacement along the principal mode. Fig. 1 *B* shows R_g values attained during the trajectory. This plot indicates the structure becomes more compact, reducing the R_g mostly during

FIGURE 1 Relationship between the fluctuations in Ca^{2+} bound nCaM and R_g. (*A*) R_g values as a function of simulation time. (*B*) Projection of the MD trajectory along the principal component of motion that describes most of the system fluctuations. (*C*) Correlation between the first principal component and the time series of R_g values during the entire simulation. (*D*) Correlation between the first principal component and the time series of R_g values during the last 2.54 ns of simulation.

the first 0.5 ns. Fig. 1 *C* shows displacement along the principal mode versus R_g, showing a strong correlation between the first principal component and R_g. All R_g values were calculated for residues 4–74, leaving out the ends to make sure that end effects do not affect the results. These three plots taken together show that from the starting structure, based on the crystal form, there is a significant reduction in R_g that is correlated with displacements along the principal mode. This observation implies that the major motion observed in the simulation is a compacting of the nCaM. The $C\alpha$ *rmsd* from the crystal form to the final simulation configuration is 3.23 Å.

The principal component analysis was then repeated with only the last 2.5 ns of the simulation to investigate the major motions after the protein is in the more compact conformation. Fig. 1 *D* shows a plot of displacement along the principal mode versus R_g and indicates a strong correlation. This result shows that even after the protein forms a compact structure, the major motion of the nCaM is an expanding and compacting, although not to the same magnitude as the initial compacting. We will show that this expansion and compaction motion involves the opening and closing of the hydrophobic cleft and thus may have functional relevance in the binding of a variety of targets.

A second Ca^{2+}-loaded nCaM simulation extending to 1 ns was performed, again starting with the crystal form. This simulation shows, from the R_g values (Fig. 2), that the structure becomes compact fairly quickly (0.5 ns), but then expanded to the R_g value seen in the crystal form. We found that the compact structure formed in this trajectory contained 6 trapped water molecules near the closed hydrophobic cleft. The compact structure formed in the first trajectory did not contained trapped water molecules in the protein interior. The cost of trapping these water molecules, although small (García and Hummer, 2000), may have induced the re-opening of the hydrophobic cleft in this short trajectory.

To assess the role of the C-domain and the helix linker in the observed expansion and compaction motion, a third Ca^{2+}-loaded simulation was performed for 2 ns, this time with the entire CaM (residues 1–147). We find that the C_α *rmsd* distance of the last configuration of CaM with the crystal structure is 7.1 Å, when all amino acids are compared. The C_α *rmsd* distance for the N and C terminal domains are 1.8 Å and 1.42 Å, respectively. We found that the linker helix is bent at amino acid 81, and that the N and C terminal domains rearrange during the simulation. The rearrangement of these domains can be quantified by the virtual dihedral angle (VDA) between the four bound Ca^{2+} ions, defined by Wriggers et al. (1998) and Pascual-Ahuir et al. (1991). We find that the VDA changes from $-134°$ in the crystal structure to an average value of $-197 \pm 10°$. The VDA changes quickly over the first 0.1 ns from -134 to $-170°$, then it maintains a value of $-174 \pm 16°$ over the next 0.5 ns, changed gradually from -174 to $-200°$ over
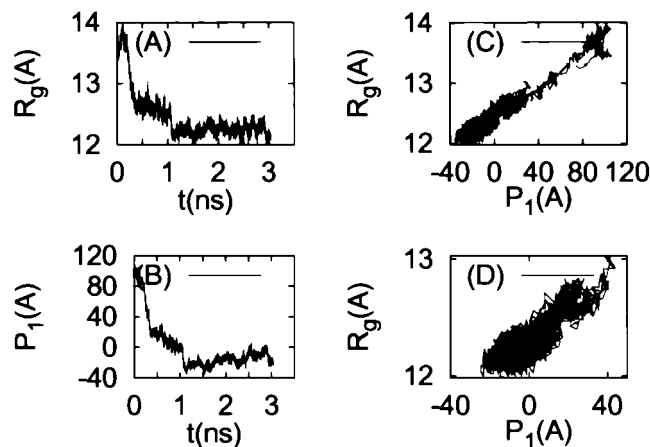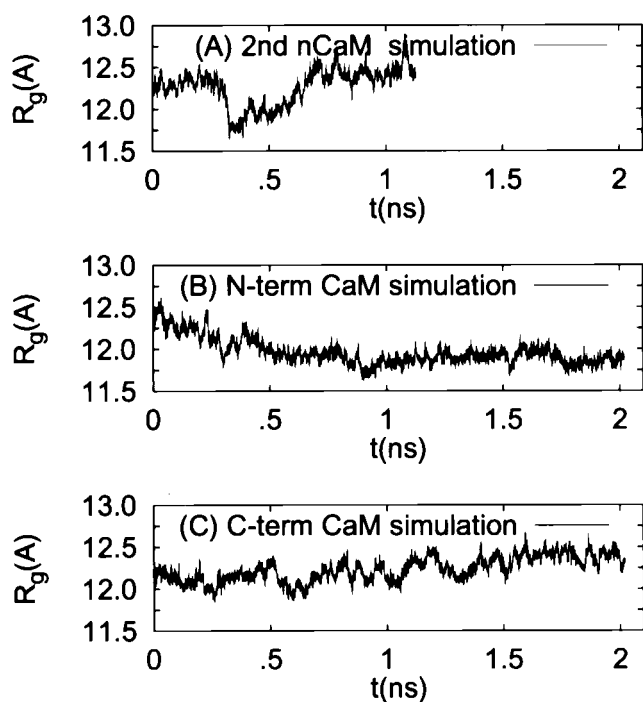
FIGURE 2 (*A*) R_g values of residues 4–74 during the second nCaM simulation (*B*) of the N- and (*C*) C-domains of CaM. For the second nCaM simulation, the structure closes at 0.4 ns, and then opens again at the end of the simulation. For the whole CaM simulation, the N-domain closes at $t = 1$ ns and remains closed for the rest of the simulation, and the C-domain shows small fluctuations around the crystal structure value.

the next 0.3 ns, and maintained an average value of $-197 \pm 10°$ over the last 1.0 ns of the 2.0-ns simulation. These results are in agreement with previous MD simulations by Wriggers et al. (1998), even though we used different force

fields, treatment of electrostatic interactions, and simulation protocols.

The R_g values for residues 4–74 during the simulation are plotted in Fig. 2. The N-domain again becomes compact, this time taking about 1 ns to become fully compact, and remains compact for the rest of the simulation. This calculation shows that the compacting is not due to some effect resulting from the absence of the C-domain. Interestingly, the C-domain does not show a compaction like the N-domain. This is in agreement with he reported NMR structure of the C-domain of CaM (Finn et al., 1995) that showed a solvent exposed hydrophobic cleft in the Ca^{2+}-loaded state.

In order to examine the nature of the compacting (i.e., reduction in R_g), we analyzed the mean square deviations of individual amino acids during the simulation. Fig. 3 *A* shows the mean square displacements (MSDs) along the optimal mode superimposed with the total MSDs of the $C\alpha$ atoms for the last 2.5 ns of the 3 ns simulation. Fig. 3 *B* shows the MSDs of the $C\alpha$ atoms along the second optimal mode. It is seen that the principal mode accounts for nearly all the major motions of the protein and therefore second and subsequent principal modes are ignored in the analysis. There are two major groups of motion in the Ca^{2+}-bound nCaM. There is a large group of motions, involving residues 30–50, with the largest motion in the middle of this group and gradually decreasing toward the ends. This region includes helix 2, helix 3, and their linker. The other large group of motion is at both ends, including most of helix 1 and helix 4. The Ca^{2+} binding loops show small structural fluctuations reflecting their tight coordination of Ca^{2+}.

Other evidence that helps us understand the compacting of nCaM can come from an examination of solvent exposure of hydrophobic groups in the cleft. Methionine residues

FIGURE 3 MSDs of the $C\alpha$ atoms for Ca^{2+}-bound nCaM. The top plot shows the MSDs along the principal component axis (blue) superimposed on the total MSDs (green). The bottom plot shows the MSDs along the second principal component axis. It can be seen that the principal component of motion accounts for almost all of the motion. The secondary structure of nCaM is as follows: Helix 1, 5–19; Ca^{2+}-binding loop 1, 20–28; helix 2, 29–37; helix linker, 38–44; helix 3, 45–55; Ca^{2+}-binding loop 2, 56–64; helix 4, 65–75.
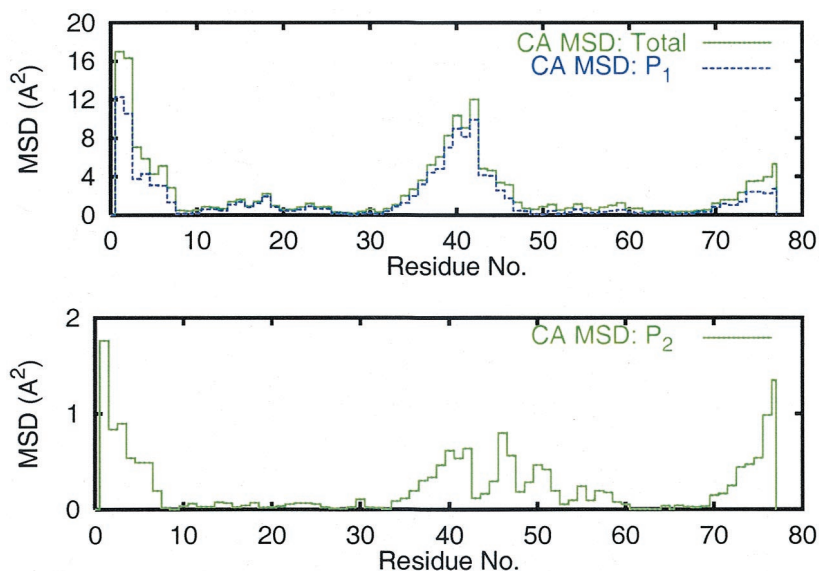
36, 51, 71, and 72 are known to be important for target binding to nCaM in its Ca^{2+}-bound form. These residues are not exposed to solvent in the apo nCaM and form part of the hydrophobic cleft region that is exposed in the Ca^{2+}-bound crystal structure. Table 1 lists water coordination values calculated from radial distribution functions of selected methionine side chain atoms (O, CB, CG, SD, CE) and for whole amino acid (obtained by the sum of proximity coordination numbers over all atoms in the amino acid and labeled "total" in Table 1). The higher the coordination number, the more exposed to solvent the atoms are. These values are calculated for the configurations sampled at the start of the Ca^{2+}-loaded nCaM simulation (close to the crystal form), during the last part of the simulation, and from the apo nCaM simulation. Only water coordination numbers >0.10 are shown. First, note that in the absence of Ca^{2+} (apo nCaM), the Met 36, 51, 71, and 72 side chains are almost completely buried and kept away from the solvent. In the first part of the Ca^{2+}-bound simulation (0.25 ns), these side chains (except Met 36) are fairly well exposed to solvent. Toward the end of the simulation, methionines 36, 71, and 72 become more buried than they were at the beginning of the simulation. However, they are not completely buried, as they are in the apo structure.

Table 2 lists interatomic distances between selected $C\alpha$ atoms, including the smallest and largest values during the simulation, and the values for the crystal form. The largest change in interatomic distance is between the end of helix 4 and residues at the end of helix 2. Met 36 on helix 2 and Met 71 on helix 4 also move relative to each other. The end of helix 4 and the beginning of helix 3 also move a fair amount relative to each other. The end of helix 2 and beginning of helix 3, however, stay more or less fixed relative to each

TABLE 1 Water coordination of methionine in the hydrophobic cleft

			nCaM: APO - 2.20 ns			
AA	O	$C\beta$	$C\gamma$	$S\delta$	$C\epsilon$	Total
M 36						0.04
M 51	0.11				0.10	0.33
M 71	0.47					0.60
M 72						0.09
			nCaM - first 0.25 ns			
M 36				0.11	0.30	0.43
M 51	0.87		0.18	0.41	0.71	2.22
M 71	0.76		0.35	0.54	0.75	2.52
M 72				0.38	0.62	1.07
			nCaM - last 2.50 ns			
M 36				0.10		0.18
M 51	0.11		0.27	0.27	0.70	1.43
M 71	0.76		0.16		0.11	1.19
M 72				0.16	0.31	0.49

TABLE 2 Interatomic distance matrix

				Smallest value during simulation				
Resid. no.	4	36	38	45	71	72	74	75
4							10.6	
36					10.0	9.7		
38				14.1				11.3
45			14.1					18.6
71		10.0						
72		9.7						
74	10.6							
75			11.3	18.6				
				Largest value during simulation				
Resid. no.	4	36	38	45	71	72	74	75
4							11.6	
36					16.0	15.7		
38				16.2				19.6
45			16.2					23.4
71		15.7						
72		16.0						
74	11.6							
75			19.6	23.4				
				Value in crystal structure				
Resid. no.	4	36	38	45	71	72	74	75
4							18.0	
36					17.4	16.4		
38				15.7				21.3
45			15.7					22.9
71		17.4						
72		16.4						
74	18.0							
75			21.3	22.9				

other. We can then see the Ca^{2+}-binding loops also stay fixed with respect to each other. A comparison between these values and Fig. 3 can yield information about the specific nature of the major motions. The end of helix 2 and beginning of helix 3 stay fixed relative to each other and the MSD indicates that this region is very mobile, slowly increasing in mobility from about residue 30, reaching a peak and then slowly decreasing until about residue 50. This result implies that helices 2 and 3 and their linker region move in a concerted fashion, pivoting about the Ca^{2+}-binding loops. Helix 1 and helix 4 also move in a concerted fashion, pivoting about the Ca^{2+}-binding loops. Since the end of helix 4 and the end of helix 2 move relative to each other, the general picture is now complete. Helices 2 and 3 and their linker move together, and helices 1 and 4 also move together. The pairs of helices thus swing toward each other and then apart, both pivoting about the Ca^{2+}-binding loops. This closing and opening of nCaM as described above explains both the change in R_g and the change in solvent exposure of the methionines. Fig. 4, *A* and *B*, illustrates the difference between the Ca^{2+}-bound open and closed structures. It is important to note that the term "closed" used here does not imply similarity to the apo
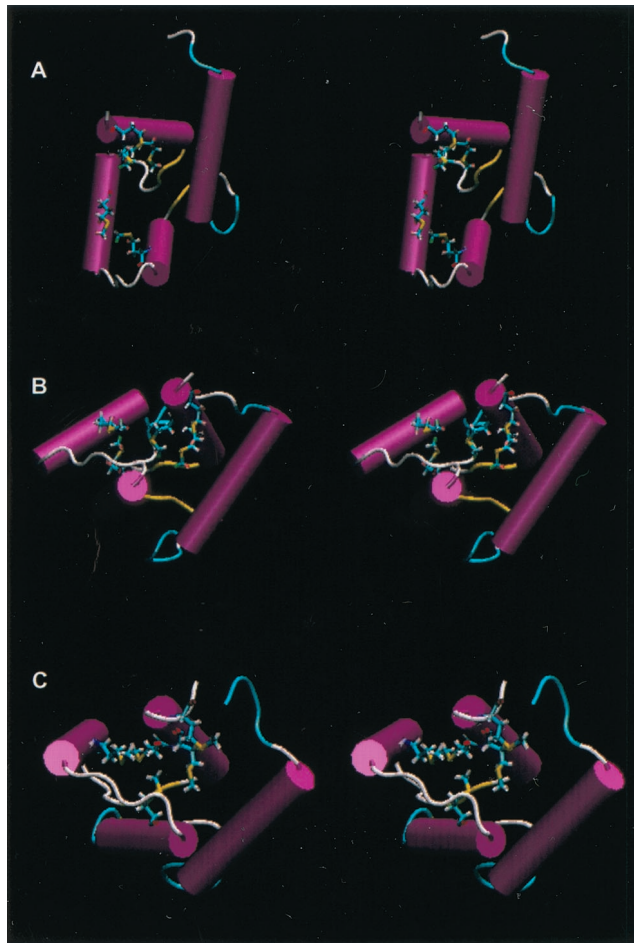
FIGURE 4 (*A*) Stereo representations of the starting configuration of the Ca^{2+}-bound nCaM MD simulation, (*B*) the final configuration, and (*C*) average apo nCaM configuration. Methionine residues that are implicated in target binding are shown explicitly. Note that there is a drastic closing of the structure during the simulation and that many key hydrophobic residues are at least partially buried from the solvent. Even though this structure is closed, as is the apo form, it is still quite different in detail from the apo form. Helical structures are defined using the program Stride (Frishman and Argos, 1995) as implemented in VMD (Humphrey et al., 1996).

nCaM. Even though the two structures give similar R_g values, the orientation of the helices relative to each other is quite different in the two (Fig. 4, *B* and *C*).

The simulation with the entire Ca^{2+}-saturated CaM also showed a closure of the N-domain that took about 1 ns to achieve and was closed and remained closed for the rest of the 2-ns simulation. This result implies that the closing and opening is not a rare event, but an equilibrium between two conformations.

Simulation on apo nCaM

The principal component analysis was performed for the apo nCaM simulation. Fig. 5 *A* shows displacement along

the principal mode of motion and Fig. 5 *B* shows R_g as a function of simulation time. One can see that there is no large compacting and expanding and that there is no correlation between the principal mode of motion and R_g. Fig. 6 *A* shows the MSD along the principal mode superimposed with the total MSDs of the $C\alpha$ atoms. Fig. 6 *B* shows the MSDs along the second principal mode. As before, almost all of the motion lies in the principal mode. The motion here is much different than for the Ca^{2+}-bound version. The most mobile regions are the Ca^{2+}-binding loops due to the lack of Ca^{2+} coordination. Also, the helix linker region and helix 3 appear to be fairly mobile. In fact, the distance between the ends of helices 3 and 4 (Ala 57 $C\alpha$ to Asp 64 $C\alpha$) that connect to Ca^{2+} binding loop 2 ranges from 15.1 to 16.30 during the simulation. In the Ca^{2+}-bound simulation, this distance is much shorter, ranging from 8.8 to 9.2 Å. On the other hand, the distance between helices 1 and 2 which connect Ca^{2+}-binding loop 1 (Leu 18 $C\alpha$ to Glu 31 $C\alpha$) ranges from 10.6 to 11.0 Å in the apo CaM simulation, which is quite close to its distances of 9.9 to 10.4 Å in the Ca^{2+}-bound simulations. Other regions of the protein are quite motionless on this time scale. On average, the structure does not change much from the NMR structure (1.87 Å *rmsd* from NMR structure to final simulation structure). The opening and closing motion seen in the Ca^{2+}-bound simulation is completely absent here.

Small-angle x-ray scattering

Fig. 7 shows the x-ray scattering data for apo- and Ca^{2+}-loaded nCaM. Table 3 gives the values of R_g, d_{max}, and V (molecular volume) for each structure, calculated from $P(r)$ analysis of the scattering data, and compares them to the values obtained for the equivalent crystal or NMR-derived structures as well as the structures from the simulations. In addition, Table 3 gives the R_g and d_{max} values obtained by modeling the scattering data using ELLMODEL, with the corresponding χ^2 values that give a measure of the quality of the model fit to the scattering data. The parameters for the structures obtained from the $P(r)$ analysis and for the best-fit model to the scattering are in excellent agreement with each other and with those obtained from the simulations. In the case of the apo-nCaM, we also see excellent agreement with the equivalent NMR solution structure. However, the R_g and d_{max} values obtained from the Ca^{2+}-loaded nCaM structure based on the crystal form are significantly larger (by 1.7 and 9 Å, respectively) than those obtained from the scattering and the simulation. Fig. 8 shows the best-fit model derived from the scattering data (green crosses) overlaid with the Ca^{2+}-loaded nCaM structure based on the crystal form before (gray ribbon) and after (red ribbon) the 3 ns simulation. The figure highlights the difference in the position of helices 1 and 4 with respect to helices 2 and 3 before and after the simulation. It also shows clearly that the model derived from the scattering data fits well the structure

FIGURE 5 (*A*) Displacement along the principal component of motion for apo nCaM during the simulation. (*B*) R_g during simulation. It is clear that there are no large changes in R_g during the simulation and that there is no correlation between R_g and the principal component of motion.
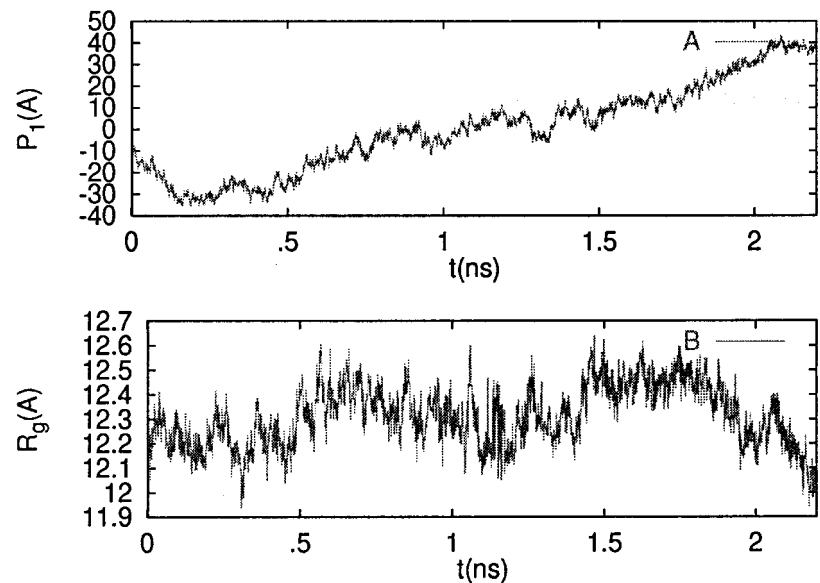
from the simulation, but not that of the crystal form, consistent with the comparison of the R_g and d_{max} values.

DISCUSSION

The combined results of our simulations and experiments provide evidence that Ca^{2+}-bound nCaM exists in both open and closed conformations. Since small-angle x-ray scattering yields information about the protein conformational ensemble in solution, we conclude that in solution, on average, the N-domain of CaM exists in a more closed conformation than that seen in the crystal structure. The results of the simulation indicate there is some exposure of hydrophobic groups to the solvent. The NMR solution structure of nCaM with 2 Ce^{3+} bound in place of Ca^{2+} has been solved, and also shows a more compact conformation than is seen in the crystal structure (Bentrop et al., 1997). However, the simulations also show that there are significant structural deviations from this average, with the principal mode of motion being a concerted opening and closing of the hydrophobic cleft. Due to the fact that the transitions from open to closed and from closed to open happen fairly quickly (Figs. 1 and 2), there is most likely only a small energy barrier between the two conformations, or a large number of conformations (substates) that span an almost continuous range of states between the open and closed hydrophobic cleft conformations. It is feasible that even small crystal packing forces could open up the nCaM to the extent seen in the crystal structure. Solution conditions, however, drive the structure, on average, more toward the closed conformation. It has previously been shown that crystal packing forces stabilize the intact CaM structure with an extended interconnecting helix region that is, in contrast, flexible in solution (Heidorn and Trewhella, 1988; Wriggers et al., 1998). Crystal packing forces could also be distorting the geometry within the N-domain. The high

FIGURE 6 MSDs of the Cα atoms for apo nCaM. The top plot shows the MSDs along the principal component axis (blue) superimposed on the total MSDs (green). The bottom plot shows the MSDs along the second principal component axis. It can be seen that the principal component of motion accounts for almost all the total motion. The secondary structure of nCaM is as follows: Helix 1, 5–19; calcium-binding loop 1, 20–28; helix 2, 29–37; helix linker, 38–44; helix 3, 45–55; Ca^{2+}-binding loop 2, 56–64; helix 4, 65–75.
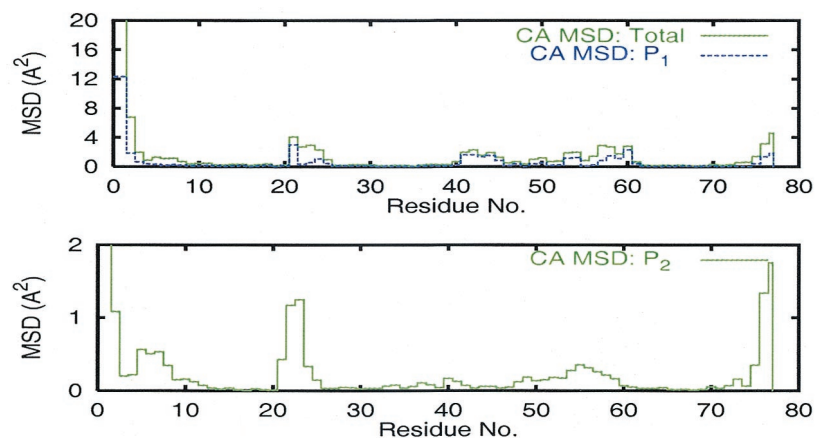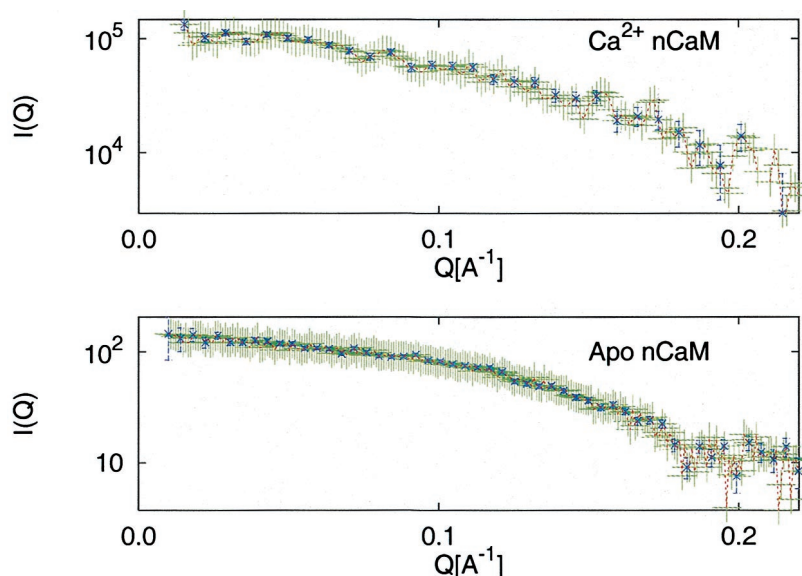
FIGURE 7   X-ray scattering data for the 1–77 nCaM with and without bound Ca^{2+} overlaid with the corresponding scattering curve calculated from the best-fit model.

resolution crystal structure of Ca^{2+}-loaded CaM analyzed in terms of multiple configurations agree with this picture, even though the displacements observed in the crystal structure are much smaller than we observed in the simulations and in x-ray scattering in aqueous solution (Wilson and Brunger, 2000).

Even though the solution structure of the Ca^{2+}-loaded nCaM is closed relative to the crystal structure, it is quite different from the apo structure as seen by NMR. In the NMR structure, apo-nCaM has its helices wrapped around each other in an almost antiparallel configuration (Kuboniwa et al., 1995). In contrast, our closed apo simulation structure shows the helices arranged more perpendicularly, as in the Ca^{2+}-bound crystal structure (Meador et al., 1992), but with helices 2 and 3 with their linker swinging about the Ca^{2+}-binding loops toward and away from helices 1 and 4, which also swing about the Ca^{2+}-binding loops (Fig. 4).

TABLE 3   Structural parameters for the nCaM: analysis of x-ray scattering data

Model	R_g (Å)	d_{max}	χ^2
Ca^{2+}-bound nCaM			
X-ray data	13.2 ± 0.03	39.0 ± 2	
Model to X-ray data	13.2	39.5	1.002
crystal structure	14.9	48.0	
MD simulation	13.4	38.5	
Apo nCaM			
X-ray data	13.2 ± 0.2	39 ± 2	
Model to X-ray data	13.2	40	1.73
NMR structure	13.2	39	
MD simulation	13.2	39	

R_g and d_{max} are calculated by Fourier transformation of $U(Q)$ to give $P(r)$, which directly gives d_{max}. R_g is calculated as the second moment of $P(r)$ (Heidorn and Trewhella, 1988).

Our closed Ca^{2+}-bound structure also shows some exposure of hydrophobic groups to solvent, whereas the apo structure shows minimal solvent exposure.

Ca^{2+} binding to the N-domain of CaM in solution thus appears to cause a rearrangement of its helices, but does not necessarily form an open structure as in the crystal structure. The major surprise, however, is the large opening and closing motion that Ca^{2+}-loaded nCaM exhibits. This motion is likely due to a competition between geometric strain in the closed conformation and unfavorable exposure of hydrophobic residues to solvent in the open conformation (Nelson and Chazin, 1998). Because this kind of opening and closing motion is completely absent in the apo simulation, it is plausible that this flexibility is important in CaM function. The NMR structure of CaM complexed the CaM-binding peptide from MLCK solved by Ikura et al. (1992) shows the N-domain even more open than it is in the Ca^{2+}-bound crystal structure with no target present (Chattopadhyaya et al., 1992). This result provides further evidence of the flexibility the Ca^{2+}-bound N-domain of CaM to open and close.

CaM binds many targets of different sizes and charge distribution, with the only pattern in sequence apparent being the placement of two hydrophobic residues separated by 12 residues in the MLCK-like binding domains, and with no other obvious sequence homology. The opening and closing of the N-domain after Ca^{2+} binds could account for the proteins ability to bind so many different targets. There are at least two possible underlying mechanisms: one is that, once the target is near, it induces CaM opening at a relatively low free energy cost. Another possibility is that the target binds when CaM moves into a metastable open conformation. Both of these mechanisms would allow for variability in target structure and for a more effective induced fit match to give tighter binding than the current model of
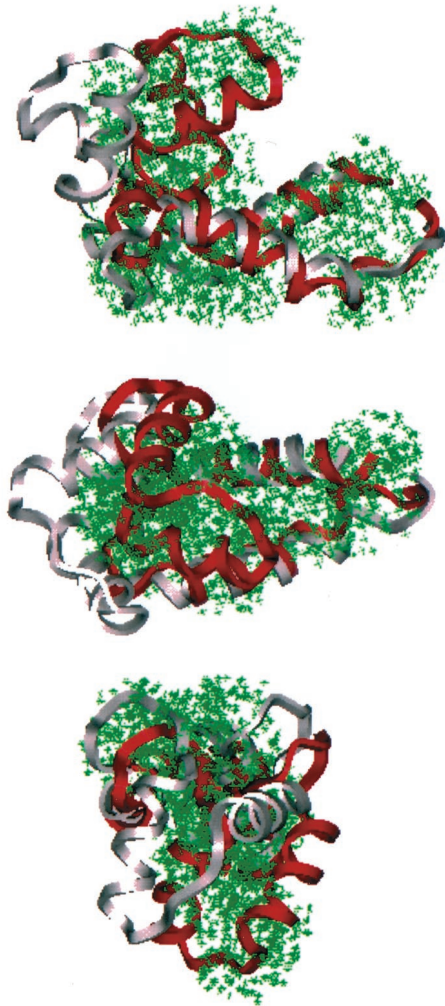
FIGURE 8   (*Top*) Three views of the crystal structure of Ca^{2+}-loaded nCaM (gray ribbon), the final simulation structure of the Ca^{2+}-loaded nCaM (red ribbon), and the best-fit model of the Ca^{2+}-loaded nCaM calculated from solution small-angle x-ray scattering data (green crosses). It is easily seen that the final simulation structure is very close in overall size and shape to the model derived from the scattering data. The crystal structure, on the other hand, is much more elongated than the others.

Ca^{2+} activation via a change in the time-averaged conformation of the domain.

It has been shown that EF hand proteins do not need to be in an open conformation to bind targets (Yap et al., 1999). For some, such as calbindin (Skelton et al., 1994) and the N-domain of cardiac troponin C (Li et al., 1999), Ca^{2+} binding does not result in a large exposure of a hydrophobic surface, but still binds target peptides with high affinity. In the case of cardiac troponin C, it is the target peptide binding itself that appears to open the N-domain (Li et al., 1999). Therefore, alternate mechanisms for target peptide binding in CaM such as those discussed above, are quite feasible. Because of great similarity of structures among EF hand proteins, it is possible that this kind of flexibility to

open and close is common to all or most EF hand proteins. Subtle differences in the position of equilibrium between open and closed conformations or the magnitude of motion among different EF hand proteins could play a role in their differing functions.

The general lack of motion in the apo nCaM during the simulation is interesting. It is expected that the Ca^{2+}-binding loops are mobile because they are a large group of uncoordinated negative charges. However, it was not expected that the rest of the structure be as static as we have seen. The simulation, lasting only 2.5 ns, provides only a very short window of conformational flexibility. It is possible that on a longer time scale, apo CaM adopts many very different conformations. On the short time scale, however, it remains fairly static. As discussed in Results, for nCaM, the ends of the helices connecting to binding site 2 are much farther apart than they are in the Ca^{2+}-bound version. Tight Ca^{2+} coordination requires these ends to come much closer. Also, the end of helix 3 connecting to binding site 2 is very flexible. Ca^{2+} binding site 1, on the other hand, is mostly formed and the helices connecting it are motionless, indicating that Ca^{2+} binding to site 1 does not have a great effect and that Ca^{2+} binding to site 2 is responsible for the majority of the conformational change.

In comparing the dynamics of the apo- and Ca^{2+}-loaded nCaM, it is tempting to speculate that the key effect of Ca^{2+} binding is to stabilize the Ca^{2+}-binding loops. This stabilization could provide a stable pivot point for the large-amplitude motions of the helices that open and close the hydrophobic cleft in order to facilitate target protein binding. Thus, the dynamics of the structure would regulate the interactions with target proteins, rather than a simple conformational change.

REFERENCES

Babu, Y., J. Sack, T. Greenhough, C. Bugg, A. Means, and W. Cook. 1985. 3-dimensional structure of calmodulin. *Nature.* 315:37–40.

Babu, Y. S., Bugg, C. E., and Cook, W. 1988. Structure of calmodulin refined at 2.2 a resolution. *J. Mol. Biol.* 204:191–204.

Barbato, G., M. Ikura, L. Kay, R. Pastor, and A. Bax. 1992. Backbone dynamics of calmodulin studied by n-15 relaxation using inverse detected 2-dimensional nmr-spectroscopy: the central helix is flexible. *Biochemistry.* 31:5269–5278.

Bentrop, D., I. Bertini, M. Cremonini, S. Forsen, C. Luchinat, and A. Malmendal. 1997. Solution structure of the paramagnetic complex of the n-terminal domain of calmodulin with two Ce^{3+} ions by ^{1}H-nmr. *Biochemistry.* 36:11605–11618.

Chacon, P., J. Diaz, F. Moran, and J. Andreu. 2000. Reconstruction of protein form with x-ray solution scattering and a genetic algorithm. *J. Mol. Biol.* 299:1289–1302.

Chattopadhyaya, R., W. Meador, A. Means, and F. Quiocho. 1992. Calmodulin structure refined at 1.7 angstrom resolution. *J. Mol. Biol.* 228:1177–1192.

Cornell, W., P. Cieplak, C. Bayly, I. Gould, K. Merz, D. Ferguson, D. Spellmeyer, T. Fox, J. Caldwell, and P. Kollman. 1995. A 2nd generation force-field for the simulation of proteins, nucleic-acids, and organic-molecules. *J. Am. Chem. Soc.* 117:5179–5197.

Crivici, A., and M. Ikura. 1995. Molecular and structural basis of target recognition by calmodulin. *Annu. Rev. Biophys. Biomol. Struct.* 24: 85–116.

Darden, T., D. York, and L. Pedersen. 1993. Particle mesh Ewald: an $N \cdot log(N)$ method for Ewald sums in large systems. *J. Chem. Phys.* 98:10089–10092.

Finn, B., J. Evenas, T. Drakenberg, J. Waltho, E. Thulin, and S. Forsen. 1995. Calcium-induced structural changes and domaim autonomy in calmodulin. *Nat. Struct. Biol.* 2:777–783.

Frishman, D., and P. Argos. 1995. Knowledge-based secondary structure assignment. *Proteins Struct. Funct. Genet.* 23:566–579.

Gallagher, S., A. Callaghan, J. Zhao, H. Dalton, and J. Trewhella. 1999. Global conformational changes control the reactivity of methane monooxygenase. *Biochemistry.* 38:6752–6760.

García, A. E. 1992. Nonlinear dynamics of proteins. *Phys. Rev. Lett.* 68:2696–2699.

García, A. E., and G. Hummer. 2000. Water penetration and escape in proteins. *Proteins Struct. Funct. Genet.* 38:261–272.

García, A. E., G. Hummer, R. Blumfield, and J. A. Krumhansl. 1997. Multi-basin dynamics of a protein in a crystal environment. *Physica D.* 107:225–239.

Gellman, S. 1991. On the role of methionine residues in the sequence-independent recognition of nonpolar protein surfaces. *Biochemistry.* 30:6633–6636.

Hait, W., and J. Lazo. 1986. Calmodulin: a potential target for cancer chemotherapeutic-agents. *J. Clin. Oncol.* 4:994–1012.

Heidorn, D., P. Seeger, S. Rokop, D. Blumenthal, A. Means, H. Crespi, and J. Trewhella. 1989. Changes in the structure of calmodulin induced by a peptide based on the calmodulin-binding domain of myosin light chain kinase. *Biochemistry.* 28:6757–6764.

Heidorn, D., and J. Trewhella. 1988. Comparison of the crystal and solution structures lf calmodulin and troponin-c. *Biochemistry.* 27: 909–915.

Herzberg, O., J. Moult, and M. James. 1986. Calcium-binding to skeletal muscle troponin C and the regulation of muscle contraction. *J. Biol. Chem.* 261:2638–2644.

Humphrey, W., A. Dalke, and K. Schulten. 1996. VMD: visual molecular dynamics. *J. Mol. Graphics,* 14:33–38.

Ikura, M., Clore, G., Gronenborn, A., G., G. Z., Klee, C., and Bax, A. 1992. Solution structure of a calmodulin-target peptide complex by multidimensional NMR. *Science.* 256:632–638.

James, P., T. Vorherr, and E. Carafoli. 1995. Calmodulin-binding domains: just 2-faced or multifaceted. *Trends Biochem. Sci.* 20:38–42.

Kawasaki, Nakayama, S., and Kretsinger, R. 1998. Classification and evolution of EF-hand proteins. *Biometals.* 11:277–295.

Krueger, J. K., G. Olah, S. Rokop, G. Zhi, J. Stull, and J. Trewhella. 1997. *Biochemistry.* 36, 6017–6023.

Krueger, J. K., G. Zhi, J. T. Stull, and J. Trewhella. 1998. Neutron scattering studies reveal further details of the Ca^{2+}/calmodulin-dependent activation mechanism of myosin light chain kinase. *Biochemistry* 37:13997–14004.

Kuboniwa, H., N. Tjandra, S. Grzesiek, H. Ren, C. Klee, and A. Bax. 1995. Solution structure of calcium-free calmodulin. *Nat. Struct. Biol.* 2:768–776.

Li, M., L. Spyranopolos, and B. Sykes. 1999. Binding of cardiac troponin-i147–163 induces a structural opening in human cardiac troponin-C. *Biochemistry.* 38:8289–8298.

Meador, W., A. Means, and F. Quiocho. 1992. Target enzyme recognition by calmodulin: 2.4 angstrom structure of a calmodulin-peptide complex. *Science.* 257:1251–1255.

Mehler, E., J. Pascualahuir, and H. Weinstein. 1991. Structural dynamics of calmodulin and tropnin-c. *Protein Eng.* 4:625–637. .

Mehrotra, P., and D. L. Beveridge. 1980. Structural-analysis of molecular solutions based on quasi-component distribution-functions: Application to [H2CO]aq at 25-degrees-c. *J. Am. Chem. Soc.* 102:4287–4294.

Moore, P. 1980. Small-angle scattering: information-content and error analysis. *J. Appl. Crystallogr.* 13:168–175.

Nelson, M., and W. Chazin. 1998. An interaction-based analysis of calcium-induced conformational changes in Ca^{2+} sensor proteins. *Protein Sci.* 7:270–282.

O'Neil, K., and W. Degrado. 1990. How calmodulin binds its targets: sequence independent recognition of amphiphilic alpha-helices. *Trends Biochem. Sci.* 15:59–64.

Pascual-Ahuir, J.-L., E. Mehler, and H. Weinstein. 1991. Calmodulin structure and function: Implication of arginine residues in the compaction related to ligand binding. *Mol. Eng.* 1:231–247.

Pearlman, D., D. Case, J. Caldwell, W. Ross, T. Cheatham, S. Debolt, D. Ferguson, G. Seibel, and P. Kollman. 1995. Amber, a package of computer-programs for applying molecular mechanics, normal-mode analysis, molecular-dynamics and free-energy calculations to simulate the structural and energetic properties of molecules. *Computer Phys. Commun.* 91:1–41.

Skelton, N., J. Kordel, M. Akke, S. Forsen, and W. Chazin. 1994. Signal-transduction versus buffering activity in Ca2+-binding proteins. *Nat. Struct. Biol.* 1:239–245.

Svergun, D. 1999. Restoring low resolution structure of biological macromolecules from solution scattering using simulated annealing. *Biophys. J.* 76:2879–2886.

Vito, P., Lacana, E., and DAdamio, L. 1996. Interfering with apoptosis: Ca2+-binding protein alg-2 and Alzheimer's disease gene alg-3. *Science.* 271:521–525.

Wall, M., S. Gallager, and J. Trewella. 2000. Large scale shape changes in proteins and macromolecular complexes. *Ann. Rev. Phys. Chem.* 51: 355–380.

Weinstein, H., and E. Mehler. 1994. Ca^{2+}-binding and structural dynamics in the functions of calmodulin. *Annu. Rev. Physiol.* 56:213–236.

Wilson, M., and A. Brunger. 2000. The 1.0 Å crystal structure of Ca^{2+}-bound calmodulin: an analysis of disorder and implications for functionally relevant plasticity. *J. Mol. Biol.* 301:1237–1256.

Wriggers, W., E. Mehler, F. Pitici, H. Weistein, and K. Schulten. 1998. Structure and dynamics of calmodulin in solution. *Biophys. J.* 74: 1622–1639.

Yap, K., J. Ames, M. Swindells, and M. Ikura. 1999. Diversity of conformational states and changes within the ef-hand protein superfamily. *Proteins Struct. Funct. Genet.* 37:499–507.

Zhang, M., T. Tanaka, and M. Ikura. 1995. Calcium-induced conformational transition revealed by the solution structure of apo calmodulin. *Nat. Struct. Biol.* 2:758–767.

Zhang, M., and T. Yuan. 1998. Molecular mechanisms of calmodulin's functional versatility. *Biochem. Cell Biol. Biochim. Biol. Cell.* 76: 313–323.

Zhao, J., E. Hoye, S. Boylan, D. Walsh, and J. Trewhella. 1998. Quaternary structures of a catalytic subunit-regulatory subunit dimeric complex and the holoenzyme of the camp-dependent protein kinase by neutron contrast variation. *J. Biol. Chem.* 273:30448–30459.